Lawrence Berkeley National Laboratory
Materials Sciences

Title

Coherent-scatterer enhancement and Klein-tunneling suppression by potential barriers in gapped graphene with chirality-time-reversal symmetry

Authors

Anwar, Farhana
Iurov, Andrii
Huang, Danhong
et al.

Coherent-scatterer enhancement and Klein-tunneling suppression by potential barriers in gapped graphene with chirality-time-reversal symmetry

Farhana Anwar[1]*, Andrii Iurov[2]†, Danhong Huang[3], Godfrey Gumbs[4,5], and Ashwani Sharma[3,6,7]

[1]*Lawrence Berkeley National Laboratory, 1 Cyclotron Rd, Berkeley, CA 94720*
[2]*Department of Physics and Computer Science, Medgar Evers College*
of the City University of New York, Brooklyn, NY 11225, USA
[3]*Air Force Research Laboratory, Space Vehicles Directorate, Kirtland Air Force Base, NM 87117, USA*
[4]*Department of Physics and Astronomy, Hunter College of the City*
University of New York, 695 Park Avenue, New York, NY 10065, USA
[5]*Donostia International Physics Center (DIPC),*
P de Manuel Lardizabal, 4, 20018 San Sebastian, Basque Country, Spain
[6]*Center for High Technology Materials, University of New Mexico,*
1313 Goddard SE, Albuquerque, NM 87106, USA
[7]*Department of Electrical and Computer Engineering,*
University of New Mexico, Albuquerque, NM 87106, USA
(Dated: September 14, 2021)

We have utilized the finite-difference approach to explore electron-tunneling properties in gapped graphene through various electrostatic-potential barriers ranging from Gaussian to a triangular envelope function in comparison with a square potential barrier. The transmission coefficient is calculated numerically for each case and applied to the corresponding tunneling conductance. It is well known that Klein tunneling in graphene will be greatly reduced in gapped graphene. Our results further demonstrate that such a decrease of transmission can be significantly enhanced for spatially-modulated potential barriers. Moreover, we investigate the effect from a bias field applied to those barrier profiles, from which we show that it enables the control of electron flow under normal incidence. Meanwhile, the suppression of Klein tunneling is found more severe for a non-square barrier and exhibits a strong dependence on bias-field polarity for all kinds of barriers. Finally, roles of a point impurity on electron transmission and conductance are analyzed with a sharp peak appearing in electron conductance as the impurity atom is placed in the middle of a square barrier. For narrow triangular and Gaussian barriers, however, the conductance peaks become significantly broadened, associated with an enhancement in tunneling conductance.

I. INTRODUCTION

Unusual properties of Dirac quasiparticles have become one of the most popular topics in fundamental research and a promising source for new application technologies [1–3] as well. Being a zero-gap semiconductor and possessing a specific chiral wave function simultaneously will result in full transparency to any potential barrier for normally-incident electrons [4,5]. A massless Dirac fermion which is scattered by an electrostatic potential is able to tunnel with certainty for normal incidence, as known Klein paradox, regardless of potential-barrier height or width. [6,7] Graphene is also known for its specific magnetic-field properties, [8–11] as well as its strong decrease of magneto-resistance [12,13] through p-n junctions [14]. While the metallic band structure and high mobility are obvious advantages of graphene, most applications in electronics requires a small and tunable bandgap [15] in order to keep its charged carriers confined within a finite area of an electronic device [16]. This feature could be achieved by opening a finite bandgap [17] which directly leads to a suppression of the Klein tunneling in graphene [18–21].

There are several efficient ways for creating a sizable (~ 100 meV and above) and tunable bandgap in graphene. Most of them are connected with adding a dielectric Si-based substrate [17] or a substrate with broken inversion symmetry between sublattices [20]. It was just recently recognized that a tunable gap can be achieved after a Dirac-cone hexagonal two-dimensional lattice has been irradiated with circularly-polarized [22–24] and off-resonance field [25–34]. In addition, strain engineering, finite-width graphene nanoribbons (GNR) systems, [35] structural and topological defects or insertion of impurity atoms can also produce a bandgap in graphene [15]. Physically, the presence and size of an induced bandgap in graphene and other hexagon lattices directly affect tunneling and transport properties [36–39], and play a crucial role in graphene-based electronics, such as field-effect transistors since their on/off current ratios [40] can be tuned through tunneling control. Meantime, the optical response of gapped graphene also acquires attractive

---

features in opto-electronics and optical spectroscopy [41]. Particularly, these responses have been proved sensitive to localized and trapped states within the bandgap of considered systems [42–44]. The effect of mesoscopic fluctuations appearing in the conductance of a gapped-graphene strip due to random electrostatic potential landscape is believed important but has not been investigated thoroughly as for gapless graphene [45]. The same goes for the effect of an electrostatic field applied across a potential barrier [46].

Although a considerable amount of research works has been published on graphene band-transport characteristics, studies on tunneling transport through a smoothly-varying potential barrier in a gapped Dirac system are much less touched upon. In fact, tunneling transport through a steep-slope potential profile, involving either single or double square barrier, is explored and reported in Refs. [47–49]. However, analytic solutions for most cases of a finite-slope barrier are still inaccessible. As a bright exception, we can mention an exact solution of the problem with a linear finite-slope barrier demonstrated in Ref. [50]. On the other hand, electron transmission in graphene and other newly discovered Dirac materials was also computed based on Wentzel-Kramers-Brillouin (WKB) semiclassical theory. [50–53] Furthermore, it has been shown within WKB theory that if electron-hole transition is considered inside a non-square potential barrier, tunneling transmission will increase with the slope of a potential profile. Technically, a smooth finite-slope potential barrier becomes more realistic since it matches better with the experimentally accessible situation [54]. Importantly, such a case also presents several intriguing phenomena and properties, e.g., Klein collimator [55] as well as a possibility for building up a collimated interferometer or reflector [56,57]. Besides, these smooth-barrier profiles also display unusual tunneling features upon applying an electric or a magnetic field [56,58–61].

For a square-shape barrier layer, approximate analytic expressions can be obtained for the transmission coefficient, as shown in Eq. (10) of our previous paper [62], including the modification from a finite bandgap for graphene. Additionally, detailed comparison has already been made between the WKB expression in Eq. (10) of our earlier paper [62] with a finite bandgap plus a tilted potential barrier and the predictions made by Cheianov and Fal'ko in Ref. [14] for a zero bandgap and a smooth p-n junction potential, including an exponential suppression for the tunneling coefficient with respect to a transverse wave number of incident electrons.

In comparison with tunneling transport of incident electrons across a potential barrier in graphene, impurity scattering [45,61–65] in gapped graphene turns out to be another important research topic that has not been extensively studied. Disorder embedded within an electrostatic-potential barrier in a gapped graphene system [66], which exhibits either disorder-assisted or disorder-impeded tunneling, is even less known to researchers. Specifically, the spatial position, strength and polarity of an embedded scatterer and its effect on tunneling conductance of electrons for various electrostatic potential barriers [45,63] have become the most important aspect because they decide whether the conductance of the system is enhanced or reduced with chosen impurity configurations. Consequently, it is of paramount importance to study the effect due to impurity scattering in gapped graphene and reveal the condition for suppressed back-scattering of incident electrons by appropriately distributing scatterers within a barrier region, and this plays a crucial part in our current work.

The key issue addressed in this paper is quantifying electron transmission and conductance across non-square potential barriers with a finite slope in gapped graphene subject to a DC electric field by using a discretized Dirac equation [67,68] based on a finite-difference method [62,69]. The finite-difference approach (FDA) was employed initially for studying field-induced sequential tunneling of electrons in quantum-well systems [66]. Later, this method was extended to calculate Klein tunneling in graphene [62] and transport properties in nanoribbon [67] and graphene strips [68]. The details about calculations of both reflection and transmission coefficients based on the FDA have been fully described in previous papers [62,67,68]. In computing the coherent-tunneling conductance for graphene electrons in the system, we have introduced an effective projected group velocity by averaging it with an obtained transmission coefficient, as presented in Eqs. (36) and (39) of our earlier paper [62] at low temperatures and under a weak longitudinal electric field. Our numerical model presented here is proven to be crucial for studying gapped-graphene system with a smooth disorder potential. Based on our established numerical model, we calculated accurately the effect of a disorder potential on electron tunneling and conductance.

The remaining part of the present paper is organized as follows. We first validate our discretized model by calculating transmission coefficient of gapped graphene in the presence of a potential barrier, and then compare the obtained numerical results with earlier analytical solution [70] in some limiting cases. By employing this numerical method, we further explore quantitatively how the barrier-potential profile, applied bias with different polarities and barrier-embedded disorder affect the conductance as a function of incident-electron kinetic energy for various graphene p-n junction (GPNJ) within a gapped monolayer graphene.

II. GENERAL FORMALISM

The low-energy states of gapped graphene can be described fully by a Dirac Hamiltonian with an additional gap term [18,70,71], given by

$$\hat{\mathcal{H}}(\boldsymbol{r}) = -iv_F \left[\hat{\boldsymbol{\Sigma}} \cdot \boldsymbol{\nabla} \right]_{(x,y)} + V_B(x)\, \hat{\Sigma}_0 + \Delta_G \, \hat{\Sigma}_z \,, \tag{1}$$

where $\hat{\Sigma}_{x,y,z}$ are three two-dimensional Pauli matrices, $\hat{\Sigma}_0$ is a 2×2 unit matrix, v_F is the Fermi velocity, Δ_G is the gap parameter, and $V_B(x)$ represents a spatially non-uniform barrier potential. For constant potential $V_B(x) = V_0$, the Dirac Hamiltonian in Eq. (1) gives rise to a finite energy bandgap $E_G = 2\Delta_G$ between the valence and conduction bands which are symmetric with respect to the Dirac point. In addition, the energy dispersions are calculated as $\varepsilon_\gamma(k) = \gamma\sqrt{(\hbar v_F k)^2 + \Delta_G^2}$ and $\boldsymbol{k} = \{k_x, k_y\}$ is a two-dimensional wave vector of electrons. For varied $V_B(x)$, however, we have $\gamma = \mathrm{sign}[\varepsilon_\gamma(k) - V_B(x)] = \pm 1$, corresponding to electron and hole states, respectively, where $\mathrm{sign}(x)$ is a sign function. This implies that the carrier could go through an electron-hole (or inverse) transition inside the barrier region.

In this paper, we will look forward to finding scattering-state solutions $\Phi_\gamma(\boldsymbol{r})$ for the Hamiltonian in Eq. (1) in the form two-component (spinor) type of wave function, i.e.

$$\Phi_\gamma(\boldsymbol{r}) = \exp(ik_y y)\,\Psi_\gamma(x) = \exp(ik_y y) \begin{bmatrix} \phi_A(\gamma, x) \\ \phi_B(\gamma, x) \end{bmatrix} \,, \tag{2}$$

where unlike gapless graphene both components rely on the electron-hole index γ.

As a special case, if $V_B(x) = V_0$ is a constant, the translational symmetry of the system is preserved in both x and y directions, and then the Hamiltonian in Eq. (1) can be greatly simplified as

$$\hat{\mathcal{H}}_g^{(0)}(k \,|\, \theta_{\mathbf{k}}) = \begin{bmatrix} V_0 + \Delta_G & \hbar v_F k_- \\ \hbar v_F k_+ & V_0 - \Delta_G \end{bmatrix} \,, \tag{3}$$

where $\boldsymbol{k} = (k_x^{(0)}, k_y)$, $k_\pm = k_x^{(0)} \pm ik_y$, $\gamma = \mathrm{sign}(\varepsilon_0(k) - V_0)$ within the barrier region, and $\varepsilon_0(k) = \hbar v_F \sqrt{(k_x^{(0)})^2 + k_y^2}$ is the given energy of an incident electron. In this case, the scattering-state wave function associated with the Hamiltonian in Eq. (3) takes the explicit form [18,71,72]

$$\Phi_\gamma^{(0)}(\boldsymbol{r}) = \frac{1}{\sqrt{2\gamma\,\delta\varepsilon_0(k)}} \begin{bmatrix} \sqrt{|\delta\varepsilon_0(k) + \Delta_G|} \\ \gamma\sqrt{|\delta\varepsilon_0(k) - \Delta_G|}\, \mathrm{e}^{i\theta_{\mathbf{k}}} \end{bmatrix} \exp(ik_x^{(0)}x + ik_y y) \,, \tag{4}$$

where $\theta_{\mathbf{k}} = \tan^{-1}(k_y/k_x^{(0)})$, $\delta\varepsilon_0(k) \equiv \varepsilon_0(k) - V_0 \geq \Delta_G$ for an electron with $\gamma = +1$ and $\delta\varepsilon_0(k) \leq -\Delta_G$ for a hole with $\gamma = -1$. Here, two components of the wave function spinor in Eq. (4) are not the same and their ratio further depends on the electron/hole index $\gamma = \pm 1$.

The introduced definition for electron/hole index γ in Eq. (4) corresponds to the case of a constant potential. However, it is important to notice that the kinetic energy of an upcoming particle is always specified in advance. In fact, in the presence of a potential $V_B(x)$, the total energy of a particle, i.e., $E = \sqrt{k_x^2(x) + k_y^2} + V_B(x)$ remains conserved during the full tunneling process, although its longitudinal momentum $k_x(x)$ varies with position x and may even becomes imaginary or zero by crossing the turning or crossing points, as discussed in Ref. [50].

Here, we concentrate on studying the electron transmission and conductance through a biased barrier of different geometries in gapped graphene. Therefore, we will limit our investigation only to experimentally-available symmetrical barrier profiles, e.g., triangular and Gaussian shapes. For this reason, we would like to compare our results first with the well-studied case having a square barrier

$$\frac{V_s(x)}{V_0} = \Theta(x)\,\Theta(W_B - x)\,, \tag{5}$$

where $\Theta(x)$ is the Heaviside unit step function, meaning $V_s(x) = V_0$ if $0 < x < W_B$ and is equal to zero otherwise. As adopted in Figs. 1 and 2, the selection of using a square potential barrier makes it simple to compare our numerical results for a general varying-slope barrier system with some known analytical cases and discern quantitatively the effect of a finite slope of a potential barrier.

Next, for comparison we would introduce a triangular barrier $V_t(x)$ with both positive and negative slopes present on its two sides, yielding

$$\frac{V_t(x)}{V_0} = \begin{cases} 0 & \text{for} & x < a\,, \\ (x-a)/(b-a) & \text{for} & a < x < b\,, \\ (c-x)/(c-b) & \text{for} & b < x < c\,, \\ 0 & \text{for} & x > c\,. \end{cases} \tag{6}$$

For our numerical computations, we will adopt a symmetric triangular barrier configuration which corresponds to $c - b = b - a$, as used in Fig. 3.

For comparison with experimentally-available setup, we also consider a (symmetric) Gaussian profile with the potential voltage profile varying according to

$$\frac{V_g(x)}{V_0} = \pm\texttt{exp}\left[-\left(\frac{x-x_0}{l}\right)^2\right]\,, \tag{7}$$

where l is employed to define the effective width $\sqrt{\pi}l$ of our barrier, x_0 is its symmetric center where the highest possible potential V_0 is reached, as employed in Fig. 3. Depending on the $\pm$ sign in Eq. (7), this profile could describe either a barrier $(+V_0)$ or a trap $(-V_0)$.

For numerical computations, using the Hamiltonian in Eq. (1) we obtain a pair of coupled scattering-state equations within the barrier region, leading to

$$\frac{\partial}{\partial x}\phi_B(x) + k_y\,\phi_B(x) = \frac{i}{\hbar v_F}\left[\varepsilon_0(k) - V_B(x) + V_d\,\delta(x-x_s) - \Delta_G\right]\phi_A(x)\,, \tag{8}$$

$$\frac{\partial}{\partial x}\phi_A(x) - k_y\,\phi_A(x) = \frac{i}{\hbar v_F}\left[\varepsilon_0(k) - V_B(x) + V_d\,\delta(x-x_s) + \Delta_G\right]\phi_B(x)\,. \tag{9}$$

In Eqs. (8) and (9), if we consider a tilted barrier under an applied electric field $\mathcal{E}_0$, we should replace $V_B(x)$ by $V_B(x) - e\mathcal{E}_0 x$ within the barrier region, where $\mathcal{E}_0$ can be either positive or negative. Additionally, k_y remains conserved during a tunneling process for all regions considered, i.e., to left of the barrier (1), $x < 0$, inside (2), $0 < x < W_B$, and to the right of the barrier (3), $x > W_B$. We also introduce in Eqs. (8) and (9) a single scatterer of strength $\pm V_d$ at the position $x = x_s$ within the barrier region $0 < x_s < W_B$. The scattering problem is such that there could be both transmitted and reflected waves with the amplitudes $t_i(\varepsilon_0)$ and $r_i(\varepsilon_0)$, $i = 1, 2$, in regions (1) and (2) but only the transmitted wave $t_3(\varepsilon_0)$ in region (3).

For a weak potential, the conservation of pseudospin for graphene electrons prohibits their inter-valley scatterings. In the presence of a strong potential barrier, however, the inter-valley scattering of graphene electrons with different pseudospins occurs, and therefore, a strong mixing of the pseudospins of graphene electrons is expected to show up within the barrier layer, as revealed clearlier by Eq. (28) of our early paper[62] in coupled FDA equations with a barrier potential for pseudospin-1/2 graphene electrons. Quantitatively, the degree of such mixing becomes strongly dependent on the sharpness of curvature of a barrier potential, including a very sharp delta-function potential for a single scatterer embedded in the barrier layer.

From a physical point of view, it is very interesting to notice that under the transformations $k_y \to -k_y$ and $\Delta_G \to -\Delta_G$ for $\phi_A(x) \to \phi_B(x)$ as well, Eq. (9) changes to Eq. (8) and vice versa. This implies a hidden chirality-time-reversal (CTR) symmetry for electron tunneling in this gapped-graphene system if its scatterer-embedded potential $V_B(x) - V_d\,\delta(x-x_s)$ remains unchanged under the barrier transformation with respect to $x \to W_B - x$ for fixed barrier width W_B, i.e., $V_B(x) - V_d\,\delta(x-x_s)$ should acquire mirror symmetry with respect to its midpoint $x = W_B/2$ under zero bias $\mathcal{E}_0 = 0$ condition.

III. RESULTS AND DISCUSSIONS

In order to ensure that our numerically-calculated results based on the finite-difference approach (FDA) are accurate and valid, we first compare them with some previously known cases having analytical solutions [70] for a square barrier with $V_B(x) = V_0 \, \Theta(x) \, \Theta(W_B - x)$. As a validation, we have presented in Fig. 1 the transmission coefficient $T(\varepsilon, \phi_{\mathbf{k}} \,|\, \mathcal{E}_0)$ for a square barrier using both our FDA results and the known analytical solutions [70], where the incidence angle $\phi_{\mathbf{k}} = \tan^{-1}(k_y/k_x)$ together with the incident kinetic energy ε are two crucial quantities in characterizing an incoming particle. [2,52,61] This direct comparison clearly indicates that the FDA will be valid for an arbitrary biased barrier-potential profile $V_B(x)$ on the order of 10^2-10^3 meV, including both Gaussian and triangular potential barriers embedded with a single scatterer.

The analytically-calculated transmission coefficients $T(\varepsilon, \phi_{\mathbf{k}} = 0 \,|\, W_B)$ for a 1D square-barrier potential $V_s(x)$ are plotted in Fig. 2 as functions of bandgap parameter Δ_G for various barrier widths W_B and incoming-particle energies ε. We see clearly from Fig. 2 that the transmission coefficient $T(\varepsilon, \phi_{\mathbf{k}} = 0 \,|\, W_B)$ for head-on collision will be completely suppressed once Δ_G exceeds an ε-dependent threshold value, which becomes largely independent of the barrier width W_B. However, this threshold value for Δ_G reduces with increasing incident-electron energy ε.

Now, we turn to numerical computations of transmission coefficient $T(\varepsilon, \phi_{\mathbf{k}} \,|\, \mathcal{E}_0)$ by introducing general FDA method, as described in Eqs. (8) and (9), for arbitrary shape of barrier-potential profiles under an applied bias field and with embedded point scatterers.

We first present results for the effect of a barrier-potential profile on the transmission coefficient $T(\varepsilon, \phi_{\mathbf{k}})$ in the absence of a bias field $\mathcal{E}_0 = 0$. We have specifically selected square, triangular and Gaussian as three distinctive barrier profiles in Fig. 3 in order to acquire a full comparison among them. From the left panel of Fig. 3, we find a great suppression of the Klein tunneling in the presence of a finite gap by a triangular-barrier potential $V_t(x)$ (red curve). Meanwhile, the transmission for this case is only limited to a very narrow angular region around $\phi_{\mathbf{k}} = 0$. For a square-barrier potential $V_s(x)$ (black curve), on the contrary, the transmission is distributed widely within a broad angular region bounded by $|\phi_{\mathbf{k}}| \le \pi/3$, and meanwhile the transmission for head-on collision at $\phi_{\mathbf{k}} = 0$ remains strong. The transmission for a Gaussian potential barrier $V_g(x)$ (brown curve) somewhat stands between the previous two cases with a limited angular distribution as well as a greatly enhanced strength at $\phi_{\mathbf{k}} = 0$ compared to a square-barrier and triangular-barrier potentials, respectively.

To get a better and conclusive understanding about the effect of different selected barrier-potential profiles on the transmission coefficient, we present in Fig. 4 the density plot for $T(\varepsilon, \phi_{\mathbf{k}} \,|\, V_B)$ as functions of incident-electron energy ε and incident angle $\phi_{\mathbf{k}}$ with varied barrier profiles. By comparing Figs. 4(a) and 4(b), we identify a main feature in this figure for the tunneling of electrons in gapped graphene, i.e., the transmission coefficient can be greatly reduced and nearly goes to zero as the incident energy approaches the barrier height at normal incidence, where the incident particle acquires a small or even imaginary momentum within the barrier region. Furthermore, the electron transmission is modified significantly for two different slowly-varying barrier profiles considered in Figs. 4(c) and 4(d). Here, many layered sharp resonant features of transmission coefficient observed in Fig. 4(b) for an under square-barrier incidence disappear in both Figs. 4(c) and 4(d), leaving only a single energy belt around $\phi_{\mathbf{k}} = 0$ in Fig. 4(d).

From a technology perspective, we know that the control of an electrical-current flow in graphene devices becomes crucial for their applications, such as current modulation and amplification and signal processing. For this reason, we compare in Fig. 5 the changes of scaled tunneling conductance $\sigma(\varepsilon \,|\, V_B)/\sigma_0$ as functions of incoming-particle energy ε in gapped graphene for three distinctive barrier profiles. As seen in Fig. 5, for ε sitting within the range of 50-230 meV, a square barrier gives rise to a square-like highest conductivity (black curve) which, however, will decrease as ε approaches $V_0 - \Delta_G = 235$ meV. For a triangular barrier (red curve), on the other hand, we find an strongly-oscillating conductance with multiple peaks and valleys in the same range. Quite differently, Gaussian barrier (brown curve) leads to a lowest weakly-oscillating conductivity for all barrier profiles considered within this energy range, but it produces a highest step-rising conductivity above this energy range. Meanwhile, unlike square barrier, the conductivity associated with either triangular and Gaussian potential barrier goes up quickly as $\varepsilon > 235$ meV although its increase is not as fast as that for square potential barrier around $\varepsilon = 350$ meV.

In Fig. 6, for three different barrier-potential profiles we compare the obtained numerical results for transmission coefficient $T(\varepsilon, \phi_{\mathbf{k}} \,|\, V_B)$ as a function of the angle of incidence $\phi_{\mathbf{k}}$ with a series of gap parameters Δ_G. For the Gaussian barrier profile in Fig. 6(b), the tunneling is confined well within a small angle region. With increasing Δ_G, the tunneling amplitude at $\phi_{\mathbf{k}} = 0$ is enhanced quickly to unity which is accompanied by the expanded angle region around $\phi_{\mathbf{k}} = 0$. Interestingly, very strong focusing of tunneling with respect to $\phi_{\mathbf{k}} = 0$ is developed for a triangular barrier profile in Fig. 6(c) which is supplemented by the appearance of two symmetric sharp side robes. Meanwhile, in this case, the tunneling amplitude at $\phi_{\mathbf{k}} = 0$ is reduced rapidly with increasing Δ_G, which further goes together

with the suppression of two side robes. For the square barrier profile in Fig. 6(a), lots of side robes occurs and their angular distributions are shrunken slowly with increasing Δ_G.

From a device point of view, tuning the tunneling conductance in gapped graphene is an effective technique and very important for its functionality and application. Here, we want to demonstrate tunable tunneling conductance in gapped graphene by applying a bias field $\mathcal{E}_0$ to a general barrier potential $V_B(x)$, which is in interplay with the opened bandgap of graphene. We start with a square barrier and present calculated polar plots of $T(\varepsilon, \phi_{\mathbf{k}} \,|\, \mathcal{E}_0)$ in Fig. 7(a)-(b) for forward and backward biases, respectively, from which we find the suppression of Klein tunneling at $\phi_{\mathbf{k}} = 0$ due to electron-hole transition resulting from a finite Δ_G chosen but it is still robust against the applied bias field $\mathcal{E}_0$. It is interesting to note that the suppression of transmission under normal incidence appears only for a positive biase but not for a negative bias, which exhibits a strong asymmetry with respect to the polarity of $\mathcal{E}_0$ or broken CTR symmetry in the system. In particular, enhancements of $T(\varepsilon, \phi_{\mathbf{k}} \,|\, \mathcal{E}_0)$ near $\phi_{\mathbf{k}} \approx \pm 90^{\mathrm{o}}$ are seen only for $\mathcal{E}_0 = -1\,\mathrm{kV/cm}$. On the other hand, there exists an insulating zero-conductance gap for incident-electron energy ε as found from Fig. 7(c)-(d), but its two edges shift in opposite directions with the polarity of $\mathcal{E}_0$. In this way, we can easily switch the electron tunneling conductance between the conducting and insulating phases in gapped graphene by properly selecting the polarity and magnitude of an applied bias field for any fixed kinetic energy of incident electrons.

Certainly, for a finite bandgap Δ_G of graphene, the tuning of tunneling conductance by an applied bias field also depends on the selected shape of a barrier-potential profile, such as a triangular or Gaussian barrier. For the triangular barrier under a reverse bias in Fig. 8(a), we find the conductance as a function of ε remains at zero for $\varepsilon < 50\,\mathrm{meV}$. However, both the dominant higher and the secondary lower conductance peaks move upwards as a function of incoming-electron energy ε with increasing $|\mathcal{E}_0|$. On the contrary, these two conductance peaks shift to lower values of ε with increasing $\mathcal{E}_0$ under forward biases, as found from Fig. 8(b). In order to gain an overall picture about the tuning of tunneling conductance $\sigma(\varepsilon, \mathcal{E}_0 \,|\, V_B)$ by a bias field $\mathcal{E}_0$ for different barrier profiles $V_B(x)$, we compare corresponding density plots of scaled $\sigma(\varepsilon, \mathcal{E}_0)/\sigma_0$ as functions of both incoming-particle energy ε and $\mathcal{E}_0$ in Figs. 9(a)-9(d). Generally speaking, the case for biased Gaussian barriers in Figs. 9(a)-9(b) only gives rise to two relatively-weak peaks in tunneling conductance $\sigma(\varepsilon, \mathcal{E}_0)$ within two separate ranges for kinetic energy ε. The bias field $\mathcal{E}_0$, on the other hand, only shifts those conductance peaks in $\sigma(\varepsilon, \mathcal{E}_0)$ downward in ε under the forward-bias condition but shifts it upward as a function of ε in the reverse-bias condition. For a triangular barrier, we find enhanced features for peak shifting both upwards and downwards with increasing $|\mathcal{E}_0|$, as displayed in Figs. 9(c)-9(d).

In the remaining part of this Section, we will address the effect of a single scatterer embedded at various positions within an unbiased barrier of different shapes on tunneling conductance of electrons in gapped graphene. In Fig. 10, we plot $\sigma(\varepsilon, V_d \,|\, V_B)/\sigma_0$ for an unbiased square barrier with different locations for a single scatterer. As a comparison, we also include the result with no scatterer in Fig. 10(a) under $\mathcal{E}_0 = 0$ for a square-barrier potential. From Fig. 10(b) with $x_s/W_B = 0.1$, we observe that $\sigma(\varepsilon, V_d)$ acquires several consecutive peaks and valleys within the low-energy range of $0.3 < \varepsilon/V_0 < 0.8$ in the presence of a single scatterer. In addition, a zero-conductance gap exists for intermediate energy range $0.8 < \varepsilon/V_0 < 1.3$, and meanwhile, a number of peaks and valleys develop for enhanced $\sigma(\varepsilon, V_d)$ in the high-energy region $1.3 < \varepsilon/V_0 < 1.8$. For $x_s/W_B = 0.5$ in Fig. 10(c) for the scatterer located right at the middle of square barrier, a sharp peak in $\sigma(\varepsilon, V_d)$ occurs at $\varepsilon/V_0 = 1$ within this zero-conductance gap, despite the sign and magnitude of V_d. For $x_s/W_B = 0.9$ in Fig. 10(d), we verify the CTR symmetry with respect to the center $x_s = W_B/2$ of a 1D barrier, i.e., $\sigma(\varepsilon, V_d)$ for a scatterer at x_s is the same as $\sigma(\varepsilon, V_d)$ for a scatterer at $W_B - x_s$.

To understand quantitatively the interplay between effects of a scatterer and the shape of a barrier-potential profile, we compare 2D plots in Figs. 11 and 12 for the scaled tunneling conductance $\sigma(\varepsilon, V_d \,|\, V_B)/\sigma_0$ of gapped graphene in the presence of a single scatterer at different positions within a triangular and Gaussian barrier regions, respectively. First, for a triangular barrier in Fig. 11, we observe a conductance peak at $\varepsilon/V_0 = 0.5$ for $x_s/W_B = 0.1$ instead of $\varepsilon/V_0 = 1$ as in Fig. 10(b). Moreover, $\sigma(\varepsilon, V_d \,|\, V_B)$ remains zero within the energy ranges of $0 < \varepsilon/V_0 < 0.4$ as well as $0.6 < \varepsilon/V_0 < 1$. As the scatterer is shifted to $x_s/W_B = 0.3$, we find a weak conductance peak appearing near $\varepsilon/V_0 = 0.5$ in Fig. 11(c). Furthermore, when $x_s/W_B = 0.5$, we reveal a new strong conductance peak for $\varepsilon/V_0 = 0.85$ in Fig. 11(d) due to constructive superposition of two individual peaks. In particular, the CTR symmetry with respect to the center $x_s = W_B/2$ of a 1D barrier in Fig. 10 is still maintained in Figs. 11(e) and 11(f) in comparison with Figs. 11(c) and 11(b), respectively, with a switched sign for V_d.

Finally, for a Gaussian barrier potential, we know from Fig. 12 that there exist two weak conductance peaks at $\varepsilon/V_0 = 0.3$ and $\varepsilon/V_0 = 0.65$ for $x_s/W_B = 0.1$ in Fig. 12(b). Meanwhile, a zero-conductance gap is still present within the energy ranges of $0 < \varepsilon/V_0 < 0.25$ and $0.25 < \varepsilon/V_0 < 0.65$. Interestingly, there is a suppression of $\sigma(\varepsilon, V_d \,|\, V_B)$ for incident energy ε below the barrier height V_0 as $x_s/W_B = 0.3$, as shown in Fig. 12(c). After x_s/W_B is increased to 0.5 at the peak position of Gaussian barrier in Fig. 12(d), the shape of $\sigma(\varepsilon, V_d \,|\, V_B)$ as a function of ε changes dramatically by displaying a high and wide constructive conductance peak at $\varepsilon/V_0 = 0.85$ accompanied by an overall enhancement

of conductance in the energy range of $\varepsilon/V_0 > 0.4$. Furthermore, the CTR symmetry associated with $x_s = W_B/2$ for a 1D barrier is retained in Figs. 12(e) and 12(f) compared to Figs. 12(c) and 12(b) with a switched sign for V_d.

IV. SUMMARY AND REMARKS

In summary, we have investigated tunneling and calculated the transmission properties of electrons across square, triangular and Gaussian potential barriers embedded with a single scatterer for gapped graphene by applying a finite-difference approach since their computations are not accessible by standard analytical solution techniques. We have also addressed the effect due to a bias and point scatterer located within the barrier. It is known that the transmission and conduction in gapped graphene are largely suppressed as the particle energy lies inside the bandgap within a barrier region. Due to the existence of a finite bandgap between valence and conduction bands, the Klein tunneling for head-on collision (i.e., with incident angle $\phi_{\mathbf{k}} = 0$) is suppressed for the case with a square-potential barrier. Simultaneously, the side resonances for electron tunneling, which are associated with finite incident angles, are also reduced significantly in gapped graphene. These suppression effects become even more pronounced for smooth barriers. However, we have demonstrated multiple ways to modify or even break this low-conduction condition and substantially improve the collimation of transmitted electron beam by employing the approach described above. Using the obtained transmission probability, we have further calculated the tunneling conductance which also displays a suppression for a finite gap in graphene. In fact, we have found that both transmission and conductance display a strong dependence on the barrier profile, its slope and curvature. Additionally, we have shown that the application of a bias field and its polarity greatly affect the nature of Klein-tunneling suppression resulting from broken CTR symmetry of the system, and at the same time shift conductance peaks in energy for all barrier types.

Under a bias field, a zero-conductance gap occurs for a square barrier in a range of selected incident-electron energy below the top of a barrier. For positive/negative bias, two edges of this zero-conductance gap are respectively dragged to lower/higher energies for incident electrons with increasing absolute value $|\mathcal{E}_0|$ of the bias. For a triangular barrier, on the other hand, we have only found one dominant and another secondary peak in higher and lower energy ranges for incident electrons, and similar behaviors of peak shifting have been seen with increasing $|\mathcal{E}_0|$. By introducing a single scatterer to an energy barrier of gapped graphene, we have revealed that its strength, polarity and position can affect effectively the conductance profile of gapped graphene. As a scatterer is moved to the midpoint (or the symmetry point) of an energy barrier, the resulting conductance always acquires either a peak within this zero-conductance gap or a significant enhancement from a constructive scattering contribution due to CTR symmetry of the system. Specifically, for a square barrier we have observed the appearance of a sharp conductance peak for $\varepsilon/V_0 \sim 1$ within the zero-conductance gap. For Gaussian and triangular potential barriers, however, such a conductance peak around $\varepsilon/V_0 \sim 0.85$ becomes much broaden, especially for a smooth Gaussian barrier with a smaller curvature.

Finally, we wish to emphasize that studying the conduction properties of gapped graphene and their possible alteration is very important and timely since the beginning for practical use of graphene in device applications has already been witnessed recently. Our results are directly associated with creating a spatial confinement for graphene electrons within designated areas of an electronic device modulated by a bias voltage. Apart from that, gapped graphene itself is also related to some newly discovered materials with an intrinsic spin-orbit gap, such as silicene, germanene and molybdenum disulfide. We believe that our current works could be implanted into these materials as well.

Acknowledgments

[1] A. K. Geim and K. S. Novoselov, in *Nanoscience and technology: a collection of reviews from nature journals* (World Scientific, 2010), pp. 11–19.
[2] A. C. Neto, F. Guinea, N. M. Peres, K. S. Novoselov, and A. K. Geim, Reviews of modern physics **81**, 109 (2009).
[3] A. K. Geim, science **324**, 1530 (2009).
[4] C. Beenakker, Reviews of Modern Physics **80**, 1337 (2008).
[5] M. Katsnelson, K. Novoselov, and A. Geim, Nature physics **2**, 620 (2006).

[6] O. Klein, Zeitschrift für Physik **53**, 157 (1929).

[7] A. Calogeracos and N. Dombey, Contemporary physics **40**, 313 (1999).

[8] M. Goerbig, Reviews of Modern Physics **83**, 1193 (2011).

[9] G. Gumbs, A. Iurov, D. Huang, and L. Zhemchuzhna, Physical Review B **89**, 241407 (2014).

[10] P. Pyatkovskiy and V. Gusynin, Physical Review B **83**, 075422 (2011).

[11] J. G. Checkelsky and N. Ong, Physical Review B **80**, 081413 (2009).

[12] D. Huang, A. Iurov, H.-Y. Xu, Y.-C. Lai, and G. Gumbs, Physical Review B **99**, 245412 (2019).

[13] W. Y. Kim and K. S. Kim, Nature nanotechnology **3**, 408 (2008).

[14] V. V. Cheianov and V. I. Fal'ko, Physical review b **74**, 041403 (2006).

[15] V. M. Pereira, V. N. Kotov, and A. C. Neto, Physical Review B **78**, 085101 (2008).

[16] C. Berger, Z. Song, X. Li, X. Wu, N. Brown, C. Naud, D. Mayou, T. Li, J. Hass, A. N. Marchenkov, et al., Science **312**, 1191 (2006).

[17] Z. H. Ni, T. Yu, Y. H. Lu, Y. Y. Wang, Y. P. Feng, and Z. X. Shen, ACS nano **2**, 2301 (2008).

[18] A. Iurov, G. Gumbs, O. Roslyak, and D. Huang, Journal of Physics: Condensed Matter **24**, 015303 (2011).

[19] M. Kindermann, B. Uchoa, and D. L. Miller, Physical Review B **86**, 115415 (2012).

[20] S. Y. Zhou, G.-H. Gweon, A. Fedorov, d. First, PN, W. De Heer, D.-H. Lee, F. Guinea, A. C. Neto, and A. Lanzara, Nature materials **6**, 770 (2007).

[21] A. Iurov, G. Gumbs, O. Roslyak, and D. Huang, Journal of Physics: Condensed Matter **25**, 135502 (2013).

[22] A. Iurov, G. Gumbs, and D. Huang, Physical Review B **99**, 205135 (2019).

[23] T. Oka and H. Aoki, Physical Review B **79**, 081406 (2009).

[24] Y. Liu, G. Bian, T. Miller, and T.-C. Chiang, Physical review letters **107**, 166803 (2011).

[25] A. Iurov, G. Gumbs, and D. Huang, Journal of Physics: Condensed Matter **32**, 415303 (2020).

[26] L. M. Pastrana-Martinez, S. Morales-Torres, V. Likodimos, J. L. Figueiredo, J. L. Faria, P. Falaras, and A. M. Silva, Applied Catalysis B: Environmental **123**, 241 (2012).

[27] G. Usaj, P. M. Perez-Piskunow, L. F. Torres, and C. A. Balseiro, Physical Review B **90**, 115423 (2014).

[28] A. Iurov, L. Zhemchuzhna, G. Gumbs, and D. Huang, Journal of Applied Physics **122**, 124301 (2017).

[29] O. Kibis, Physical Review B **81**, 165433 (2010).

[30] A. Pervishko, O. V. Kibis, S. Morina, and I. Shelykh, Physical Review B **92**, 205403 (2015).

[31] M. Portnoi, O. Kibis, and M. R. Da Costa, Superlattices and Microstructures **43**, 399 (2008).

[32] O. Kibis, K. Dini, I. Iorsh, and I. Shelykh, Physical Review B **95**, 125401 (2017).

[33] A. Iurov, G. Gumbs, and D. Huang, Journal of Modern Optics **64**, 913 (2017).

[34] B. Dey and T. K. Ghosh, Physical Review B **98**, 075422 (2018).

[35] L. Brey and H. Fertig, Physical Review B **73**, 235411 (2006).

[36] K. Kristinsson, O. V. Kibis, S. Morina, and I. A. Shelykh, Scientific reports **6**, 1 (2016).

[37] M. R. Masir, P. Vasilopoulos, and F. Peeters, Physical Review B **79**, 035409 (2009).

[38] M. Zarenia, J. Pereira Jr, G. Farias, and F. Peeters, Physical Review B **84**, 125451 (2011).

[39] A. Iurov, L. Zhemchuzhna, D. Dahal, G. Gumbs, and D. Huang, Physical Review B **101**, 035129 (2020).

[40] T. Low and J. Appenzeller, Physical Review B **80**, 155406 (2009).

[41] T. G. Pedersen, A.-P. Jauho, and K. Pedersen, Physical Review B **79**, 113406 (2009).

[42] V. M. Pereira, F. Guinea, J. L. Dos Santos, N. Peres, and A. C. Neto, Physical review letters **96**, 036801 (2006).

[43] G. Gumbs, A. Balassis, A. Iurov, and P. Fekete, The Scientific World Journal **2014** (2014).

[44] E. V. Castro, N. Peres, J. L. dos Santos, A. C. Neto, and F. Guinea, Physical review letters **100**, 026802 (2008).

[45] A. Rycerz, J. Tworzydło, and C. Beenakker, EPL (Europhysics Letters) **79**, 57003 (2007).

[46] M. S. Jang, H. Kim, Y.-W. Son, H. A. Atwater, and W. A. Goddard, Proceedings of the National Academy of Sciences **110**, 8786 (2013).

[47] D. Dahal and G. Gumbs, Journal of Physics and Chemistry of Solids **100**, 83 (2017).

[48] E. Azarova and G. Maksimova, Physica E: Low-dimensional Systems and Nanostructures **61**, 118 (2014).

[49] J. Navarro-Giraldo and C. Quimbay, Journal of Physics: Condensed Matter **30**, 265304 (2018).

[50] E. Sonin, Physical Review B **79**, 195438 (2009).

[51] G. S. Paraoanu, New Journal of Physics **23**, 043027 (2021).

[52] A. Laitinen, G.-S. Paraoanu, M. Oksanen, M. F. Craciun, S. Russo, E. Sonin, and P. Hakonen, Physical Review B **93**, 115413 (2016).

[53] N. Weekes, A. Iurov, L. Zhemchuzhna, G. Gumbs, and D. Huang, Physical Review B **103**, 165429 (2021).

[54] N. Stander, B. Huard, and D. Goldhaber-Gordon, Physical review letters **102**, 026807 (2009).

[55] F. Libisch, T. Hisch, R. Glattauer, L. Chizhova, and J. Burgdörfer, Journal of Physics: Condensed Matter **29**, 114002 (2017).

[56] A. F. Young and P. Kim, Nature Physics **5**, 222 (2009).

[57] K. Wang, M. M. Elahi, L. Wang, K. M. Habib, T. Taniguchi, K. Watanabe, J. Hone, A. W. Ghosh, G.-H. Lee, and P. Kim, Proceedings of the National Academy of Sciences **116**, 6575 (2019).

[58] A. E. Mouhafid and A. Jellal, arXiv preprint arXiv:1303.0559 (2013).

[59] A. V. Shytov, M. S. Rudner, and L. S. Levitov, Physical review letters **101**, 156804 (2008).

[60] F. Anwar, C. Carlos, V. Saraswat, V. Mangu, M. Arnold, and F. Cavallo, Aip Advances **7**, 115015 (2017).

[61] F. Anwar (2020).

[62] F. Anwar, A. Iurov, D. Huang, G. Gumbs, and A. Sharma, Physical Review B **101**, 115424 (2020).

[63] M. Titov, EPL (Europhysics Letters) **79**, 17004 (2007).

[64] C. Valagiannopoulos, Physical Review B **100**, 035308 (2019).

[65] T. Ando and M. Koshino, Phys. Rev. Lett **53**, 2449 (1984).

[66] D. Huang, A. Singh, and D. Cardimona, Physics Letters A **259**, 488 (1999).

[67] A. R. Hernández and C. H. Lewenkopf, Physical Review B **86**, 155439 (2012).

[68] J. Tworzydło, C. Groth, and C. Beenakker, Physical Review B **78**, 235438 (2008).

[69] D. Huang, F. Anwar, A. Iurov, G. Gumbs, and A. Sharma, Bulletin of the American Physical Society **65** (2020).

[70] M. Setare and D. Jahani, Physica B: Condensed Matter **405**, 1433 (2010).

[71] P. Pyatkovskiy, Journal of Physics: Condensed Matter **21**, 025506 (2008).

[72] A. Iurov, G. Gumbs, D. Huang, and L. Zhemchuzhna, Journal of Applied Physics **121**, 084306 (2017).
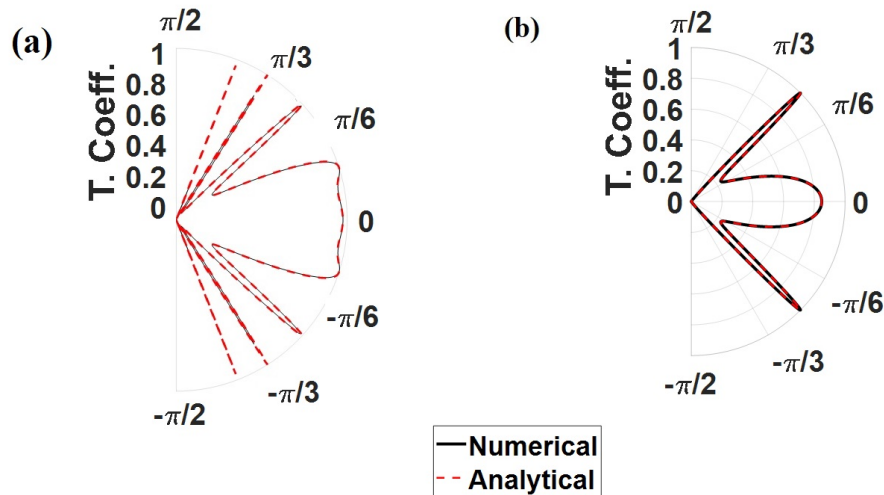
FIG. 1: (color online) Polar plots for the transmission coefficient $T(\varepsilon, \phi_{\mathbf{k}} \,|\, W_B)$ as a function of incidence angle $\phi_{\mathbf{k}}$ in graphene with a bandgap $\Delta_G = 50\,\mathrm{meV}$ for a square potential barrier $V_s(x) = V_0\,\Theta(x)\,\Theta(W_B - x)$ with various barrier widths W_B. Here, both the analytical expressions (solid curves) and numerical results (dashed curves) obtained by using the FDA method are plotted together for comparisons. Panel (a) displays calculated $T(\varepsilon, \phi_{\mathbf{k}} \,|\, W_B)$ for $W_B = 110\,\mathrm{nm}$, while panel (b) shows $T(\varepsilon, \phi_{\mathbf{k}} \,|\, W_B)$ for $W_B = 50\,\mathrm{nm}$, where the barrier height is $V_0 = 285\,\mathrm{meV}$, the bias field $\mathcal{E}_0 = 0$, and the incident-electron energy $\varepsilon = 80\,\mathrm{meV}$ are assumed.
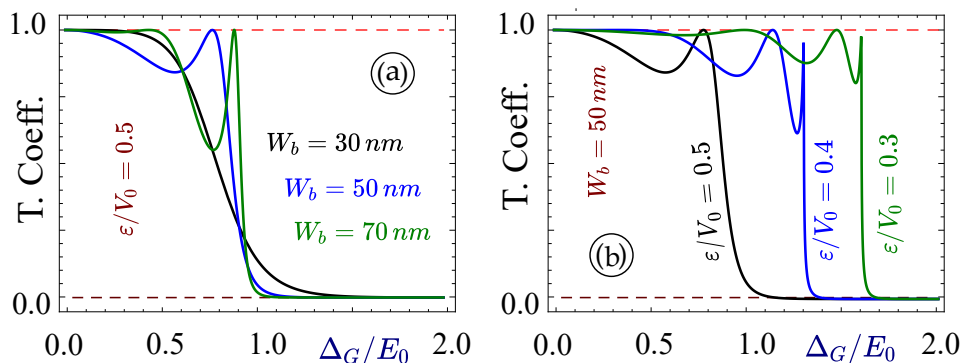
FIG. 2: (color online) Calculated transmission coefficients $T(\varepsilon, 0 \,|\, W_B)$ for the head-on collision $\phi_{\mathbf{k}} = 0$ through a square-barrier potential $V_s(x)$ as functions of bandgap parameter Δ_G with various barrier widths W_B in panel (a) and with different incident-electron energies ε in panel (b). Here, $V_0 = 0.2\,\mathrm{eV}$ and the unit-energy $E_0 = 0.1\,\mathrm{eV}$ are chosen for both panels.
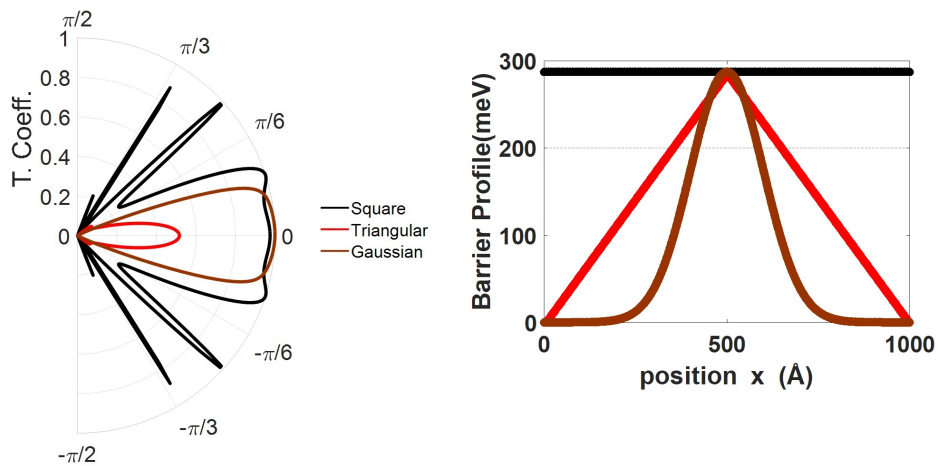
FIG. 3: (color online) (Left) comparison of the FDA calculated transmission coefficients $T(\varepsilon, \phi_{\mathbf{k}})$ as a function of the angle of incidence $\phi_{\mathbf{k}}$ for three different unbiased barrier-potential profiles with $V_0 = 285$ meV, $\mathcal{E}_0 = 0$, $\Delta_G = 50$ meV, and $\varepsilon = 80$ meV, including a square (black), a triangular (red) and Gaussian (brown) potential barrier. (Right) corresponding potential-barrier profiles $V_B(x)$ chosen for our computation results presented in the left panel.
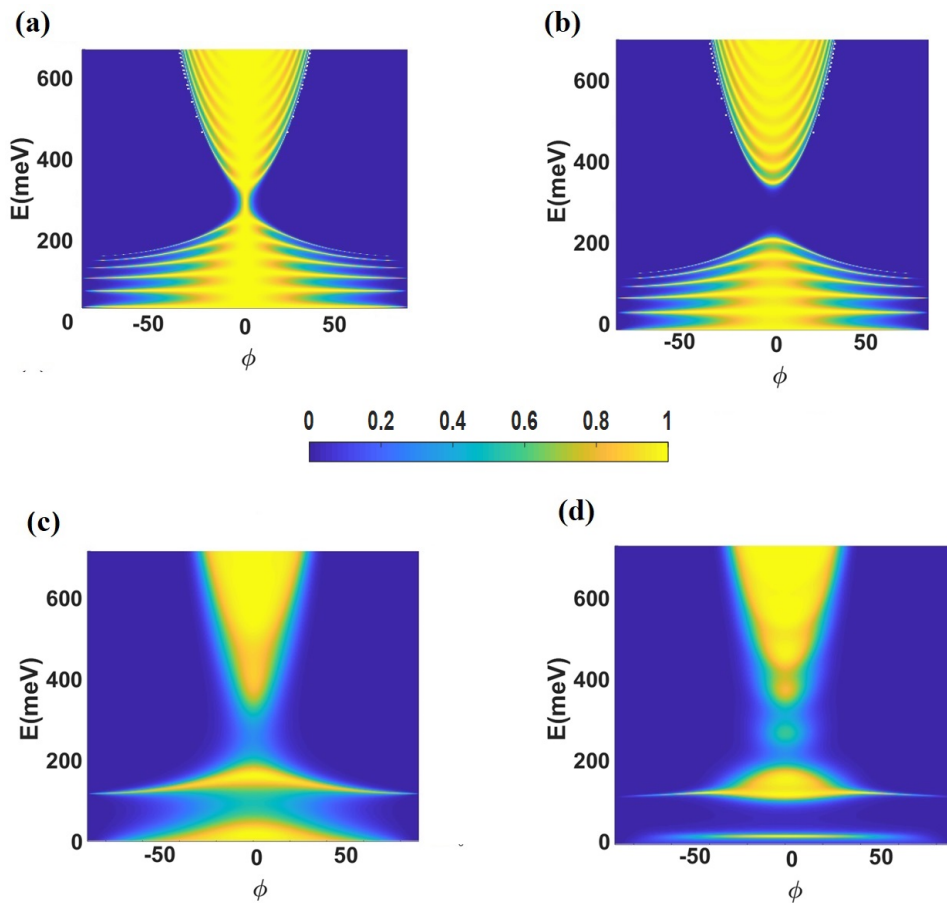
FIG. 4: (color online) Density plots for the transmission coefficient $T(\varepsilon, \phi_{\mathbf{k}} \,|\, V_B)$ as a function of the incoming-particle energy ε and incidence angle $\phi_{\mathbf{k}}$ for various barrier profiles $V_B(x)$ in four different cases: (a) a square barrier without gap; (b) a square barrier with a gap $\Delta_G = 50$ meV; (c) a triangular barrier with a gap $\Delta_G = 50$ meV; (d) Gaussian potential barrier with a gap $\Delta_G = 50$ meV. For all plots, the bias field $\mathcal{E}_0 = 0$, the barrier width is $W_B = 110$ nm, and its height is $V_0 = 285$ meV.
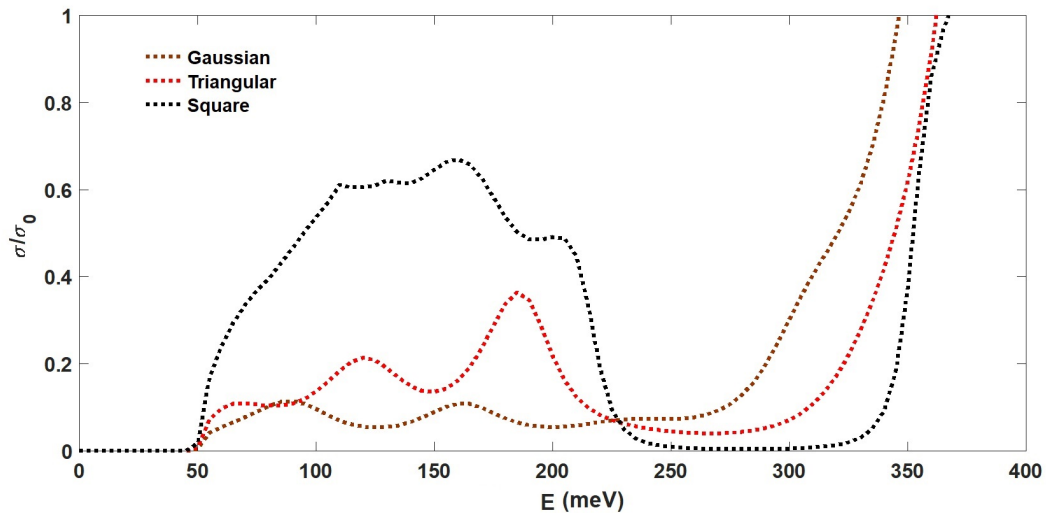
FIG. 5: (color online) Relative conductance σ/σ_0 as a function of the incident-electron energy ε for three different barrier profiles, i.e., square (black), triangular (red) and Gaussian (brown) as depicted, in gapped graphene. Here, we set the barrier height $V_0 = 285\,\mathrm{meV}$, the barrier width $W_B = 100\,\mathrm{nm}$, the gap parameter $\Delta_G = 50\,\mathrm{meV}$, and the bias field $\mathcal{E}_0 = 0$, similar to those used in Fig. 3. The unit for the conductance is chosen to be $\sigma_0 = 2\,e^2/\pi\hbar$.
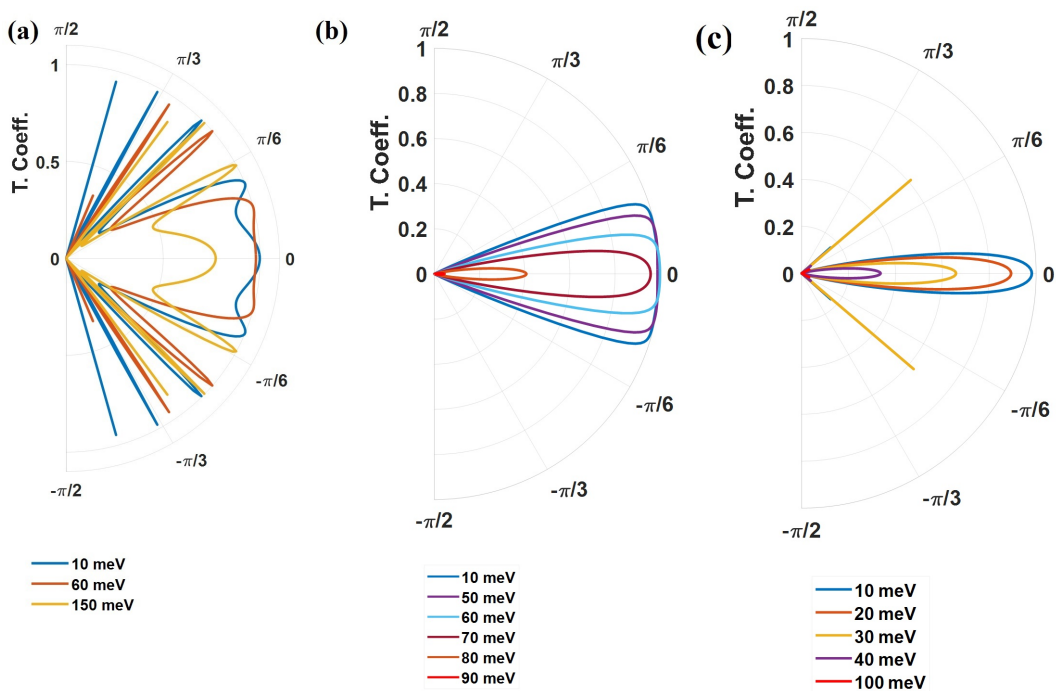
FIG. 6: (color online) Transmission coefficient $T(\varepsilon, \phi_\mathbf{k}\,|\,V_B)$, calculated by FDA method, as a function of the angle of incidence $\phi_\mathbf{k}$ for various bandgaps in graphene and different barrier profiles $V_B(x)$: (a) square barrier; (b) Gaussian barrier; (c) triangular barrier. Here, we set the barrier width $W_B = 110\,\mathrm{nm}$, the barrier height $V_0 = 285\,\mathrm{meV}$, the bias field $\mathcal{E}_0 = 0$, and the incident-electron energy $\varepsilon = 80\,\mathrm{meV}$.
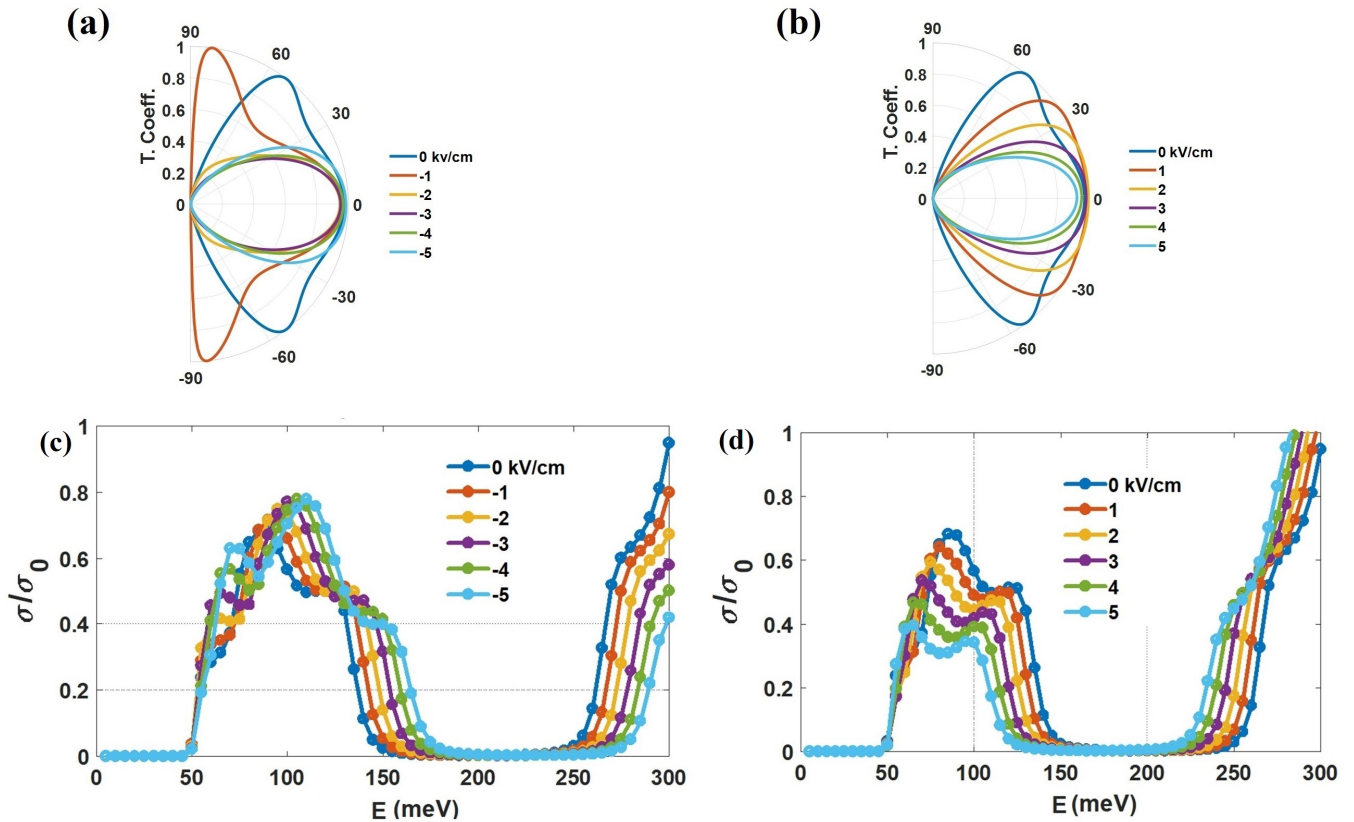
FIG. 7: (color online) Polar plots of $T(\varepsilon, \phi_{\mathbf{k}} \,|\, \mathcal{E}_0)$ as a function of $\phi_{\mathbf{k}}$ for gapped graphene with $\Delta_G = 50$ meV over a square barrier with its height $V_0 = 285$ meV, width $W_B = 110$ nm, as well as various applied bias fields $\mathcal{E}_0$. Here, Panels (a)-(b) show the results for fixed $\varepsilon = 80$ meV corresponding to a reverse and a forward bias, respectively. Panels (c)-(d) display the change of relative conductance σ/σ_0 as functions of ε for a reverse and forward bias, separately. The unit for the conductance in panels (c) and (d) is $\sigma_0 = 2e^2/\pi\hbar$.
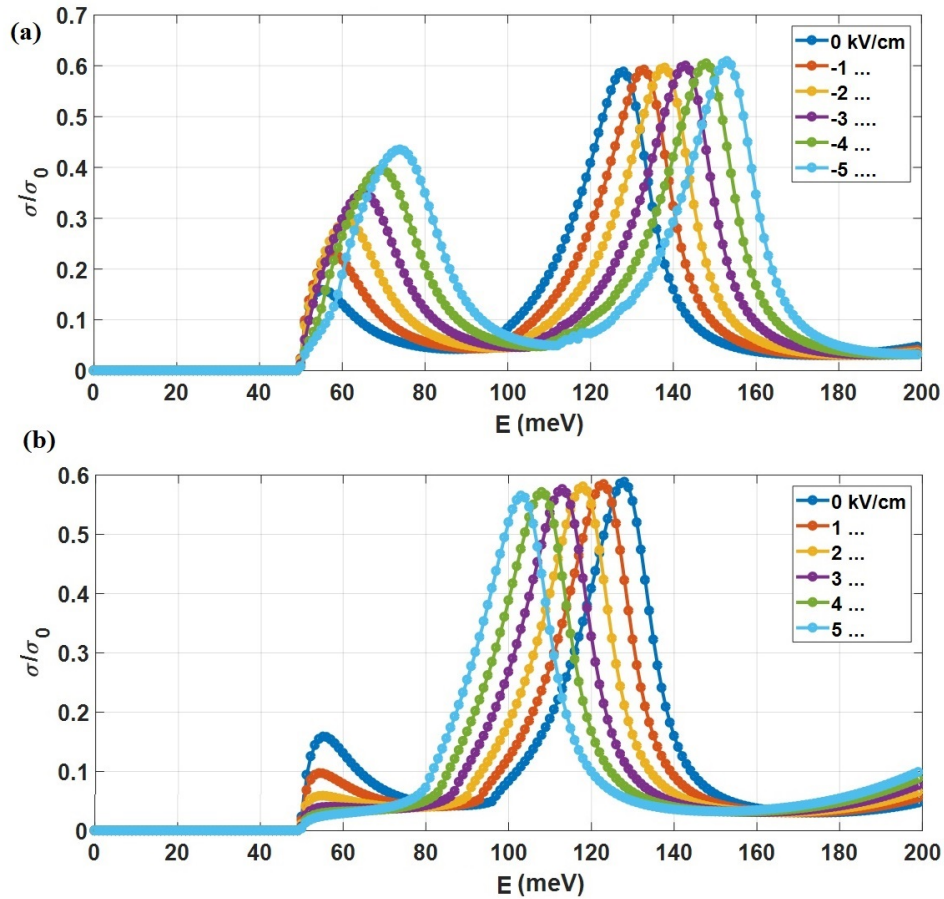
FIG. 8: (color online) Numerically-calculated relative conductance σ/σ_0 as a function of $\phi_{\mathbf{k}}$ for gapped graphene with $\Delta_G = 50\,\text{meV}$ over a triangular barrier with its height $V_0 = 285\,\text{meV}$, width $W_B = 110\,\text{nm}$, as well as various applied bias fields $\mathcal{E}_0$. Panels (a) and (b) display the change of relative conductance σ/σ_0 as functions of ε for a reverse and a forward bias, separately. The unit for the conductance in these two panels is $\sigma_0 = 2e^2/\pi\hbar$.
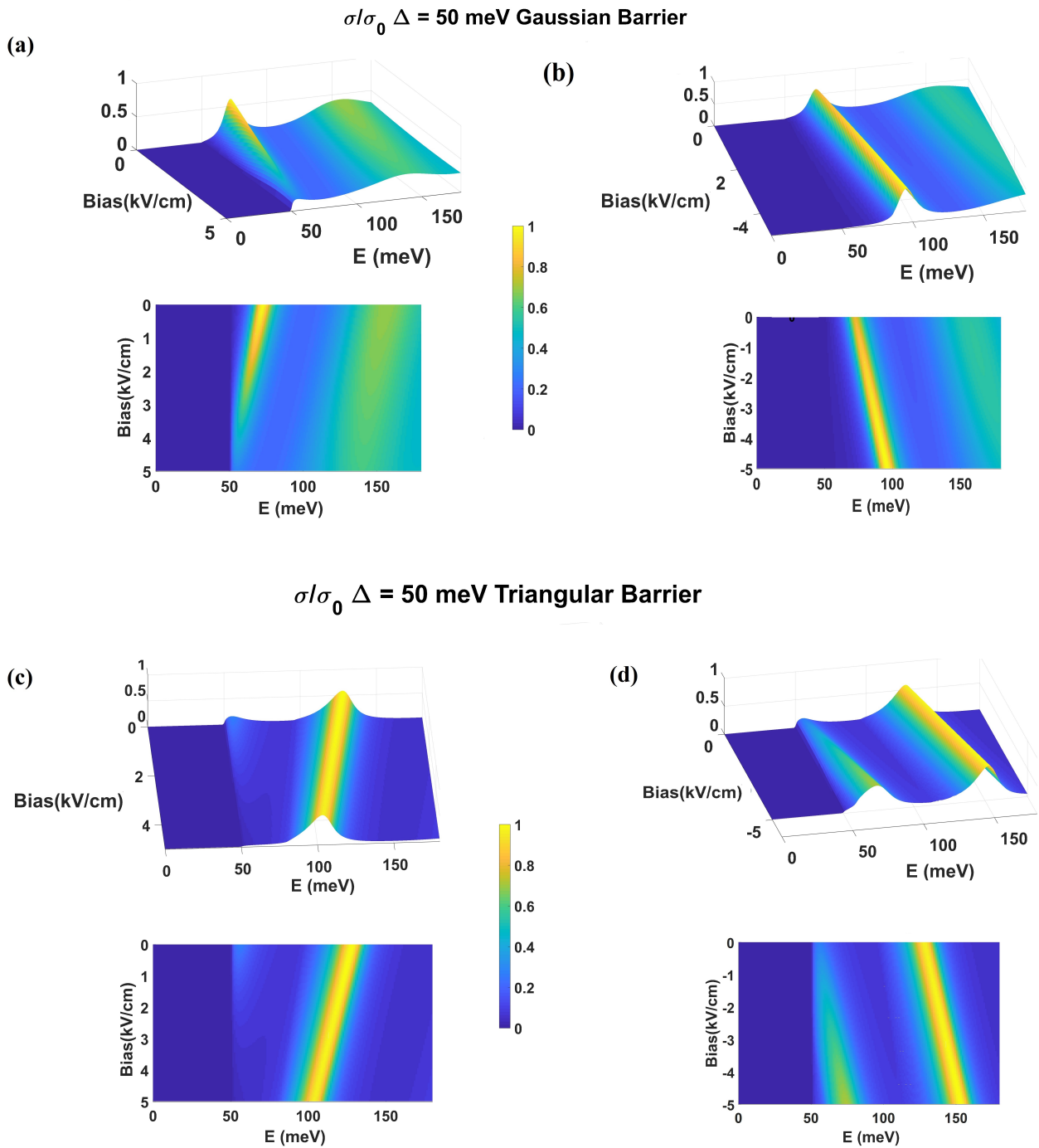
FIG. 9: (color online) 2D plots of tunneling conductance as functions of applied bias $\mathcal{E}_0$ and incident-electron energy ε. Here, four panels correspond to (a) Gaussian barrier with forward bias; (b) Gaussian barrier with reverse bias; (c) triangular barrier with forward bias; (d) triangular barrier with reverse bias. For all cases, we choose the barrier width $W_B = 110$ nm, the barrier height $V_0 = 285$ meV, and the energy gap $\Delta_G = 50$ meV. The unit for the conductance in panels (a)-(d) is set as $\sigma_0 = 2e^2/\pi\hbar$.
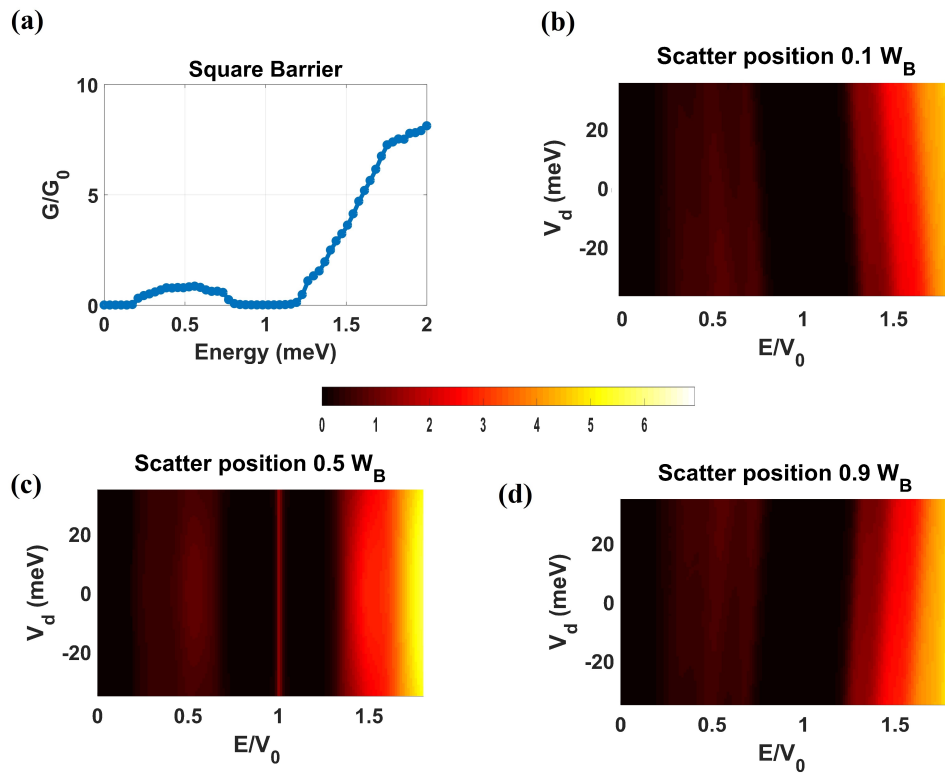
(a)

(b)

(c)

(d)

FIG. 10: (color online) 2D plots for σ/σ_0 as functions of incident energy ε and scattering strength V_d (both positive and negative) for the case of a square barrier with width $W_B = 100\,\mathrm{nm}$, height $V_0 = 285\,\mathrm{meV}$ and zero bias $\mathcal{E}_0 = 0$. Here, panel (a) presents the result for the situation with no scatterer, while panels (b)-(d) correspond to σ/σ_0 with a single scatterer sitting at various positions $x_s/W_B = 0.1, 0.5, 0.9$. The unit for the conductance in panels (a)-(d) is set as $\sigma_0 = 2e^2/\pi\hbar$.
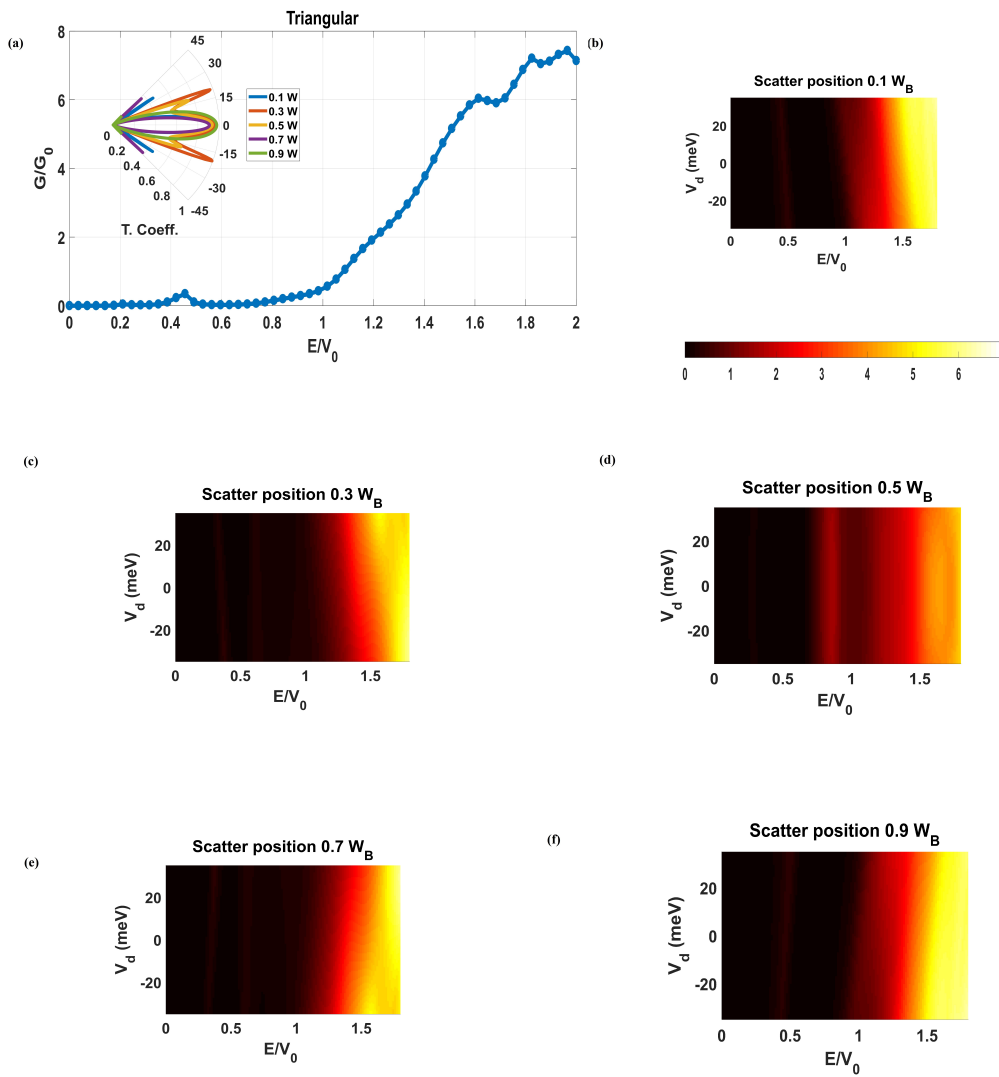
FIG. 11: (color online) 2D plots for σ/σ_0 as functions of incident energy ε and scattering strength V_d (both positive and negative) for the case of a triangular barrier with width $W_B = 100\,\text{nm}$, height $V_0 = 285\,\text{meV}$ and zero bias $\mathcal{E}_0 = 0$. Here, panel (a) presents the result for the situation with no scatterer, while panels (b)-(f) correspond to σ/σ_0 with a single scatterer sitting at various positions $x_s/W_B = 0.1$, 0.3, 0.5, 0.7, 0.9, respectively. The unit for the conductance in panels (a)-(f) is set as $\sigma_0 = 2e^2/\pi\hbar$.
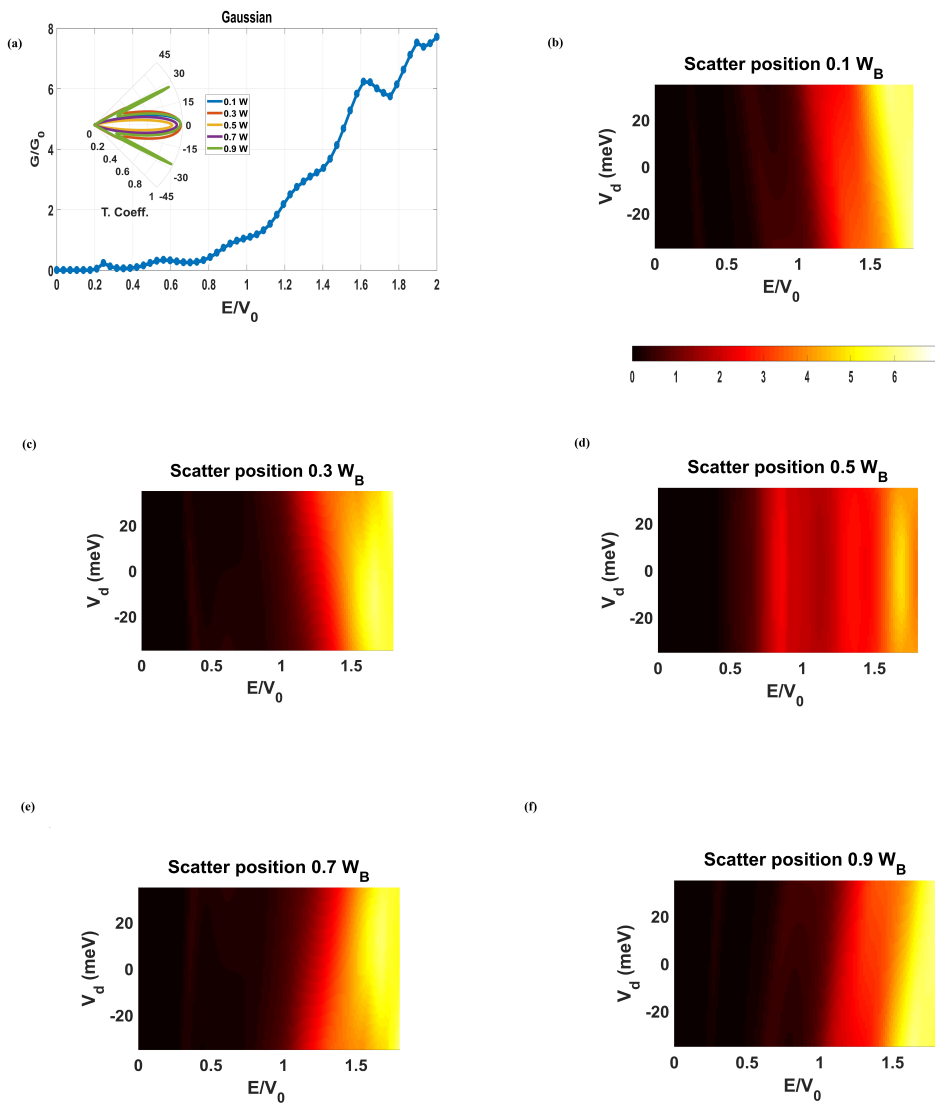
FIG. 12: (color online) 2D plots for σ/σ_0 as functions of incident energy ε and scattering strength V_d (both positive and negative) for the case of Gaussian barrier with width $W_B = 100\,\text{nm}$, height $V_0 = 285\,\text{meV}$ and zero bias $\mathcal{E}_0 = 0$. Here, panel (a) presents the result for the situation with no scatterer, while panels (b)-(f) correspond to σ/σ_0 with a single scatterer sitting at various positions $x_s/W_B = 0.1$, 0.3, 0.5, 0.7, 0.9, respectively. The unit for the conductance in panels (a)-(f) is set as $\sigma_0 = 2e^2/\pi\hbar$.